A comparative study on fracture toughness calculation models in spherical indentation tests (SITs) for ductile metals

Tairui Zhang [a,b,c], Shang Wang [a,b,c], Weiqiang Wang [a,b,c,*]

[a] *School of Mechanical Engineering, Shandong University, Jinan 250061, China*
[b] *Engineering and Technology Research Center for Special Equipment Safety of Shandong Province, Jinan 250061, China*
[c] *Research Center of Safety Guarantee and Assessment to Special Equipment, Shandong University, Jinan 250061, China*

ARTICLE INFO

ABSTRACT

The study aimed to verify the effectiveness of fracture toughness calculation models in spherical indentation tests (SITs). Four representative models, the Haggag toughness (HT) model, critical indentation energy (CIE) model, critical stress-strain (CSS) model, and energy release rate (ERR) model, which were developed on different assumptions, were selected, and experiments were performed on 10 kinds of ductile metals. A comparison proved that none of the four models provide acceptable predictions for all experimental materials. The HT model provided the best fracture toughness K_{IC} calculation for TC4, but failed for 6061 and some steels, while the other three models failed in predicting the K_{IC} of TC4. The ERR model provided an overall acceptable prediction (with a maximum error around 20%, except for TC4) while the maximum errors in the other three models exceeded (or reached) 40% for steels and 6061. Errors were investigated from the effectiveness of empirical values used in each model, which proved that the stress ratio exhibits the best consistency and thus explained the reason why the ERR model provides the best fracture toughness calculations. The reason why the K_{IC} of TC4 cannot be calculated with continuum-damage-mechanics based CIE and ERR models was also clarified through an investigation on its fracture (damage) mechanism through SEM observations. Further investigation proved that the fracture toughness can also be calculated from uniaxial tensile tests with an application of the CSS or ERR model, which verified the universality of these two models.

1. Introduction

Fracture toughness, which indicates a material's resistance to crack propagation, has great importance in structural integrity evaluations. However, conventional fracture toughness tests, such as the compact tension (CT) and three points bending, all need destructive sampling and sophisticated operations (e.g., fatigue pre-cracking and crack length measurements), and thus cannot be used on in-service structures. The spherical indentation test (SIT), due to its non-destructive and easy performance, has been widely investigated [1, 2] and has been successfully used in predicting the uniaxial mechanical properties of materials [1, 3-5]. However, when it comes to fracture toughness calculation, the problem becomes complicated.

No macro-crack is induced during a SIT on ductile metals, and thus the first problem lies in the interpretation of why unnotched indentation specimen can be used to determine the fracture toughness that originally belonged to notched ones. Despite the fact that the indentation specimen locates in a concentrated stress state, similar as its CT counterparts [6], the differences between compressive (in SITs) and tensile (in CT tests)

stress states cannot be neglected. The differences between the damage/fracture behavior under a tensile and compressive stress state have been witnessed and proved in many previous studies [2, 7, 8], but most previous studies only concentrated on the damage and fracture under a tensile stress state. There are very limited researches [8, 9] regarding the damage/fracture mechanism of ductile metals under a compressive stress field, let alone its damage/fracture mechanism. Hopefully, the introduction of shear damage into GTN model [10-12], provides insights into the damage evolution and prediction, and has achieved success in predicting the reduction of effective Young's modulus and the damage location [13-15]. The successful application of the shear modified GTN model also validates the key role of shear in SITs, and this should be considered in fracture toughness calculation and interpretation.

During the last two decades, several fracture toughness calculation models [16-21] based on different assumptions were proposed to correlate the indentation test with its conventional counterparts, but no comparative studies were performed to verify their effectiveness and accuracy on a variety of engineering metals, and this may cause confusion of which model should be selected when performing a SIT.

Nomenclature

a	contact radius, mm
a_{eff}	effective contact radius, mm
a_{max}	maximum contact radius, mm
A_{eq}	equivalent crack area, mm^2
c^2	pile-up (or sink-in) coefficient
D	damage variable
D_{Cri}	critical damage variable
D_{Cri}^{II}, D_{Cri}^{II}	critical damage variable from shear and tensile tests
E, E_{ind}	Young's modulus of specimen and indenter materials, GPa
E_{eff}	effective Young's modulus, GPa
E_P	strength coefficient, MPa
E_0	Young's modulus of virgin material, GPa
h	indentation depth, mm
h_c	actual indentation depth, mm
h_{Cri}	critical indentation depth, mm
h_{max}, h_p, h_r	maximum, plastic, and reloading depth, mm
h^*	normalized indentation depth
h_{Cri}^*	normalized critical indentation depth
H_{IT}	indentation hardness, MPa
J_{IC}, J_{IIC}	critical J under Mode I and II loading, N mm^{-1}
J_{SIT}	energy release rate from a cyclic SIT, N mm^{-1}
J_{Ten}	energy release rate from a cyclic tensile test, N mm^{-1}
K_{IC}	fracture toughness, MPa m$^{0.5}$
K_{IIC}	critical stress intensity factor under Mode II loading, MPa m$^{0.5}$
L	characteristic length, mm
n	hardening exponent
p_m	mean contact pressure, MPa
P	indentation load, N
P_{max}	maximum indentation load, N
r_C	critical plastic zone radius, mm
R	radius of spherical indenter, mm
R_m	tensile strength, MPa
$R_{p0.2}$	proof strength at 0.2% plastic strain, MPa
R_0	radius of residual indentation, mm
S	unloading slope, N mm^{-1}
S_0	theoretical unloading slope, N mm^{-1}
U_R	tensile resilience, MPa
U_D	damage strain energy, N mm
v, v_{ind}	poisson's ratio of specimen and indenter materials
W_F	energy required to form unit area crack, N mm^{-1}
W_{IEF}	indentation energy to fracture, N mm^{-1}
W_{IEF}^*	normalized indentation energy to fracture, MPa
W_P	plastic work performed at the crack tip, N mm^{-1}
W_T	temperature dependent portion of W_F, N mm^{-1}
W_0	temperature independent portion of W_F, N mm^{-1}

Greek letters

ε_f, ε_p, ε_t	fracture, plastic, and true strain
σ_{max}	maximum normal stress, MPa
σ_t	true stress, MPa
σ_{Tri}	stress triaxiality
τ_{max}	maximum shear stress, MPa
α	stress ratio
ψ	indentation governing factor
φ	plastic zone development indicator

The study aimed to (1) verify the effectiveness of different fracture toughness calculation models in SITs that were developed on different assumptions, (2) investigate the source of errors in each model, as well as the possible solutions to reduce the calculation errors, and (3) discuss the possibility for applying the calculation models to other unnotched specimens (e.g., uniaxial tensile specimens).

2. Fracture toughness calculation models

2.1. Haggag toughness (HT) model

Based on the assumptions that the fracture toughness can be interpreted as the deformation capability of the material under a concentrated stress field, the indentation test generates a concentrated stress field that is similar to that ahead of a crack tip under Mode I loading (despite that indentation stress fields are mostly compressive). The concept of indentation energy to fracture (IEF) W_{IEF} was proposed in 1998 [22].

$$W_{IEF} = \int_0^{h_{Cri}} p_m \, dh \tag{1}$$

$$p_m = \frac{P}{\pi a^2} \tag{2}$$

where p_m is the mean contact pressure, P is the indentation load, a is the contact radius, and h and h_{Cri} are the indentation depth and its critical value, respectively. It is worth noting that p_m has the same definition as indentation hardness H_{IT}, and thus measures the hardness of specimen materials [23].

The energy W_F required to form a unit area crack in a ductile metal can be described as:

$$W_F = W_0 + W_T \tag{3}$$

where W_0 is determined by the surface energy and the elastic properties of the material (independent of the test temperature), while W_T is determined by the plastic properties and is closely related to the test temperature. For ductile metals, W_T is much larger than W_0, and thus W_F can be approximated as:

$$W_F \approx W_T = W_{IEF} \tag{4}$$

According to the Griffith theory, the fracture toughness K_{IC} can be determined with:

$$K_{IC} = \sqrt{2EW_F} \tag{5}$$

where E is the Young's modulus of the specimen material. Despite the fact that the concept IEF (as well as the definition W_{IEF}) is purely empirical, it has been widely used [6, 24, 25], and generally two judgments for determination of the h_{Cri} were proposed in previous studies.

Based on experiments on carbon and ferritic steels, a simple critical fracture strain/stress model, which defines the depth h when the plastic strain reaches 12% (or true stress reaches 800 MPa) as its critical value for all ductile metals, was proposed by Haggag [22, 26] (named as the Haggag toughness model, abbreviated as the HT model). The plastic strain and true stress during a SIT can be calculated with Eqs. (6) and (7), respectively:

$$\varepsilon_p = 0.2 \frac{a}{R} \tag{6}$$

$$\sigma_t = \frac{P}{\pi a^2 \psi} \tag{7}$$

where ψ is the indentation governing factor and varies from 1.1 to 2.87 according to the development of the plastic zone beneath the spherical indenter, and R is the radius of spherical indenter.

$$\psi = \begin{cases} 1.12 & \varphi \leq 1 \\ 1.12 + 0.53 \ln \varphi & 1 < \varphi \leq 27 \\ 2.87 & \varphi > 27 \end{cases} \tag{8}$$

$$\varphi = \frac{\varepsilon_p E_{ind}}{0.43 \sigma} \tag{9}$$

where φ is a factor that indicates the development of the plastic zone and E_{ind} is Young's modulus of the indenter material.
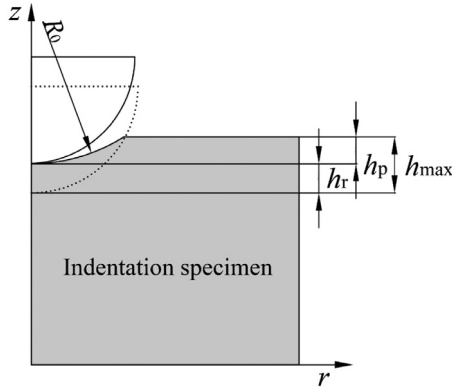
Fig. 1. Illustration of the residual spherical surface.
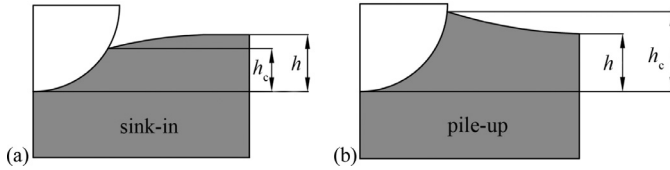

Fig. 2. The phenomenon of (a) sink-in and (b) pile-up .

2.2. Critical indentation energy (CIE) model

For a better interpretation of the fracture toughness calculation with unnotched indentation tests, continuum damage mechanics was introduced by Lee in 2006 [6], and the Critical Indentation Energy to Fracture (CIE) model was proposed. The critical indentation depth in Eq. (1) was defined as the depth when the damage variable D reaches its critical value D_{Cri}. In continuum damage mechanics, the damage variable can be determined through the variation of Young's modulus [27].

$$D = 1 - \frac{E_{eff}}{E_0} \tag{10}$$

where E_0 is the Young's modulus of the virgin material (material before damage). E_{eff} is the effective Young's modulus (Young's modulus of the damaged material), and can be determined from the unloading slope with the revised Pharr-Oliver model proposed in a previous study [28].

$$E_{eff} = \frac{1 - v^2}{2\sqrt{\frac{h_r R R_0}{R_0 - R}} / S - \left(1 - v_{ind}^2\right) / E_{ind}} \tag{11}$$

where v and v_{ind} is the Poisson's ratio of the specimen and indenter materials, respectively. R_0 is the radius of residual spherical surface and h_r is the reloading depth, as shown in Fig. 1, and can be calculated with Eqs. (12), and (13), respectively.

$$R_0 = \frac{h_p^2 + \left(2h_{max}R - h_{max}^2\right)}{2h_p} \tag{12}$$

$$h_r = h - h_p \tag{13}$$

where h_{max} and h_p are the maximum and plastic indentation depths, respectively. To ensure an elastic reloading, h_r cannot exceed $(h_{max} - h_p)$ and its maximum value was used in this study (e.g., $h_r = h_{max} - h_p$, which indicates the beginning of unloading or the final of elastic reloading). The phenomenon of sink-in and pile-up, as shown in Fig. 2(a) and (b), respectively, may cause a deviation between the measured values from the displacement sensor h and the actual depth h_c (depth that takes the sink-in and pile-up amount into consideration).

In previous studies [29, 30], the pile-up (or sink-in) coefficient c^2, as shown in Eq. (14) is used to describe the amount of pile-up (or sink-in)

during a SIT.

$$c^2 = \frac{h_c}{h} \tag{14}$$

where $c^2 > 1$ indicates a phenomenon of pile-up, otherwise, the sink-in happens. As the value of c^2 is closely related with the flow property of a material, it should be calibrated from FE calculations of the indentation test [4, 23].

To verify the similarity between a SIT and a conventional fracture toughness test, finite element (FE) calculations were performed [6]. The calculations proved that variation of the stress triaxiality beneath the spherical indenter and ahead of a crack tip are similar. However, the comparison only focused on their absolute values, and the fact that the stress triaxiality beneath the spherical indenter is negative while that ahead the crack tip is positive was neglected. Studies by French and Weinrich [31], Bao and Wierzbicki [7, 32], and Zhang et al. [2] all proved that the damage mechanism of ductile metals at high stress triaxiality or a negative one is totally different. Therefore, the direct application of D_{Cri} from a mode I fracture test (or a uniaxial tensile test) to a SIT is questionable. A possible understanding is that the critical damage variable from shear tests D_{Cri}^{II} can be correlated with the tensile one D_{Cri}^{I} with Eq. (15) according to the simple relation between the Young's modulus and modulus of rigidity [33].

$$\frac{1 - D_{Cri}^{I}}{1 - D_{Cri}^{II}} = \sqrt{\frac{3}{2(1 + v)}} \tag{15}$$

D_{Cri}^{II} should be used as SITs share the same shear damage mechanism [2] with pure shear tests. In the original work of Lee [6], D_{Cri}^{I} was concluded from finite element (FE) calculations by Andersson [34] on the voids growth and coalescence ahead of a moving crack tip under Mode I loading. The FE calculations were only for perfectly plastic materials, and thus may cause problems when the experimental materials exhibit obvious hardening behaviors. Additionally, failure was assumed to occur when the plastic zones of two adjacent voids touch each other. However, previous studies [8, 35] proved that the failure of two adjacent voids sources from several conditions, e.g. void linkage due to internal necking, simple touching, void sheeting, and void growth and linkage in materials with large and small inclusions, and thus it is questionable to simply attribute the failure ahead of a moving crack tip under mode I loading to only simple touching . As D_{Cri}^{I} may also be empirically determined from cyclic uniaxial tensile tests and was proved to be a value around 0.17–0.24 [36], D_{Cri}^{II} used in SITs can be roughly considered as a constant 0.25 when D_{Cri}^{I} and v are constant 0.2 and 0.3, respectively.

2.3. Critical stress-strain (CSS) model

Based on fracture and contact mechanics, another critical stress-strain model (abbreviated as the CSS model) was proposed by Jeon in 2016 [18]. Similar to Haggag's suggestions, the fracture criterion was separately discussed according to the specimen materials. In the critical strain case, it was assumed that the energy release per unit crack length is balanced by the amount of plastic work performed ahead of the crack tip, and thus the plastic work W_P performed at the crack tip can be given as:

$$W_P = 2r_C \left(\frac{dW}{dV}\right)_C \tag{16}$$

where r_C is the critical plastic zone radius at which a stable crack extension begins ahead of the crack tip and $(dW/dV)_C$ is the critical strain energy density obtained from a uniaxial tensile test. As the J-integral is strongly related to the plastic behavior of materials at the crack tip, Jeon [18] assumed that the critical J_{IC} before a crack propagates is equal to the critical plastic work.

$$J_{IC} = W_P \tag{17}$$

The fracture toughness of a material can then be calculated with Eq. (18).

$$K_{IC} = \sqrt{\frac{E}{1-v^2} J_{IC}} \qquad (18)$$

The stress-strain curve of specimen material can be calculated with Eqs. (6) and (7), and the critical plastic zone radius r_C of a ductile metal can be calculated from an empirical correlation with the tensile resilience U_R [18].

$$r_c = 0.10947 U_R^{0.3594} \qquad (19)$$

$$U_R = \frac{R_{p0.2}^2}{2E} \qquad (20)$$

where $R_{p0.2}$ is the proof strength at 0.2% plastic strain. The critical strain energy density $(dW/dV)_C$ indicates the area under a stress-strain curve and can be approximated by:

$$\left(\frac{dW}{dV}\right)_C \approx \frac{R_{p0.2} + R_m}{2} \varepsilon_f \qquad (21)$$

where R_m and ε_f are the tensile strength and true fracture strain of the sample material, respectively. The method to evaluate ε_f from a SIT was provided in a previous study [28]. For relatively brittle metals, J_{IC} is defined as:

$$J_{IC} = \int_0^{h_{Cri}} p_m dh \qquad (22)$$

where h_{Cri} is defined as the depth when $p_m = 4.83 R_{p0.2}$, and J_{IC} in Eq. (22) has the same definition (with a different critical criterion) as W_{IFE} in Eq. (1). However, no method to distinguish whether the stress or the strain one should be used for an unknown (or degraded) material was given in the CSS model [18].

2.4. Energy release rate (ERR) model

The three calculation models mentioned above equate the external work (or the strain energy density) at a critical status (with applications of different criterions) to the work needed to form a unit crack area, and similar assumptions were also adopted in other studies [17, 21]. However, these studies failed to explain the reason why unnotched specimens can be used to calculate the fracture toughness that originally belonged to notched ones, and the critical status needs to be empirically determined. An investigation of the damage and fracture mechanism in notched specimens proved that the crack does not immediately propagate but is caused by the linkage of accumulated damage (voids and micro-cracks) [2]. As a similar damage evolution also exists in unnotched specimens [8, 28], Zhang [2] validated the feasibility to use unnotched specimens to determine the fracture toughness of a material. Based on the assumptions that the crack does not significantly propagate when the fracture toughness is determined (0.2 mm offset of the blunting line) through a conventional notched specimen and the crack measured is mainly contributed by the damage evolution ahead the crack tip, the energy release rate (ERR) model was proposed [2].

An illustration of the damage strain energy U_D (e.g. the strain energy increases due to material damage) calculated from one indentation cycle is provided in Fig. 3, in which curve OAB was experimentally measured. Here it was assumed that there is a damage 'recovery' after totally unloading (at point B), E_{eff} recovers to E_0, and thus the reloading curve can be theoretically determined (with a substitution of E_{eff} with E_0) with Eq. (11). When reloading reaches the maximum load, damage occurs and evolves to the same state before previous unloading (the critical damage under this stress state), and thus the unloading curve should still be curve AB. This damage evolution is similar to the crack propagates in a dead loaded cracked plate [35], and the area denoted by the triangle BCA indicates U_D.

$$U_D^{(i)} = \frac{1}{2} P_{max}^{(i)} \left(h_{max}^{(i)} - h_p^{(i)} - \frac{P_{max}^{(i)}}{S_0^{(i)}} \right) \qquad (23)$$
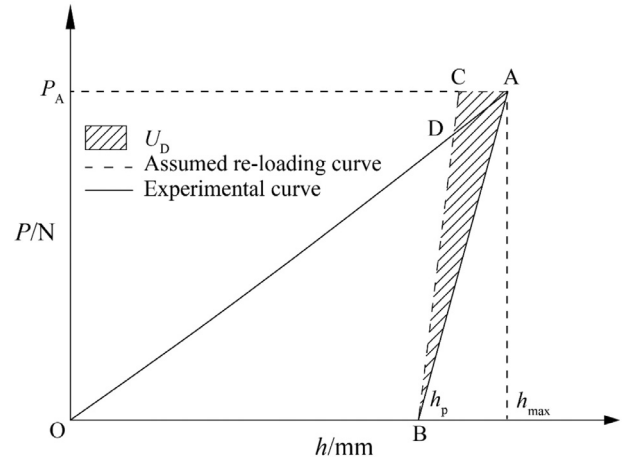

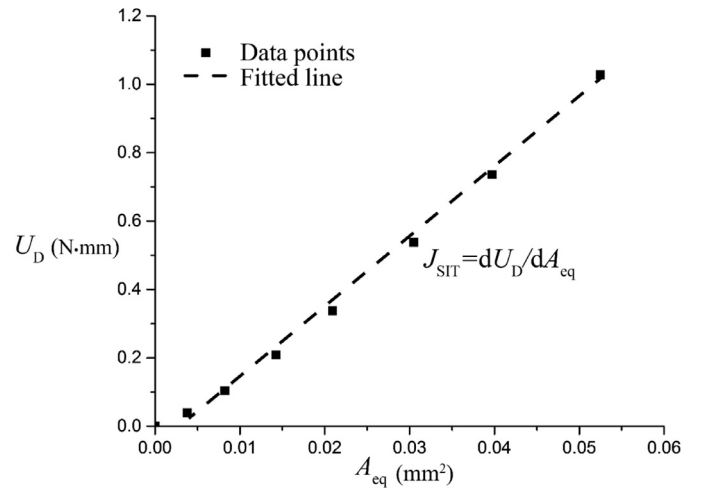**Fig. 3.** Damage strain energy U_D from one indentation cycle.

Fig. 4. Illustration of the J_{SIT} fitted from A_{eq}-U_D plot.

where the superscript (i) indicates the ith cycle and S_0 is the theoretically determined unloading/reloading slope with E_0, as the curve BC in Fig. 3. The equivalent crack area in the ith cycle $A_{eq}^{(i)}$ can be calculated with Eq. (24).

$$A_{eq}^{(i)} = \pi a_{eff}^2 D^{(i)} \qquad (24)$$

where a_{eff} is the effective contact radius that has been defined in our previous study [2], and it can be calculated with:

$$a_{eff} = \sqrt{\frac{h_r R R_0}{R_0 - R}} \qquad (25)$$

An illustration of the A_{eq}-U_D plot from a cyclic SIT is provided in Fig. 4, and the energy release rate J_{SIT} can be determined through a linear fitting of the A_{eq}-U_D plot. The damage mechanism of a ductile metal is determined by the stress state (characterized by stress triaxiality σ_{Tri}) it locates [7, 32]. When the material is located in a high stress triaxiality ($0.4 \le \sigma_{Tri}$), the damage mainly comes from the debonding of second phase particles from matrix (named as the tensile damage mechanism), while the damage comes from the dislocation pile-up (named as the shear damage mechanism) when the material is located in a low stress triaxiality ($\sigma_{Tri} \le 0$). Therefore, the energy release rate from a SIT J_{SIT} should be correlated with that in a Mode II fracture test J_{IIC} as both of them share the shear damage mechanism.

The critical stress intensity factor in Mode II loading K_{IIC} and the fracture toughness can then be determined with Eqs. (26) and (27),

Table 1
Chemical composition of experimental metals.

| Materials	C	Si	Mn	Mo	P	Cr	Ni	S	Al
18Mn	0.130	0.260	1.250	0.500	0.005	0.160	0.150	–	–
15Cr	0.148	0.313	0.500	0.511	0.005	0.922	0.122	0.001	0.040
KMN-S	0.146	0.298	0.568	1.017	0.010	2.322	0.117	0.004	–
Q345R	0.167	0.256	1.410	–	0.019	0.014	0.006	0.007	0.023
S30408	0.048	0.479	1.170	0.049	0.036	18.33	8.248	0.004	–
SA508	0.226	0.194	1.475	0.469	0.007	0.227	0.956	0.001	0.008
SA516	0.220	0.265	1.272	–	0.017	0.046	0.009	0.004	0.027
SA533	0.195	0.282	1.409	0.524	0.013	0.203	0.684	0.001	0.013
Materials	Si	Fe	Cu	Mn	Mg	Cr	Zn	Ti	
6061	23.6	0.7	0.30	0.15	1.10	0.35	0.25	0.15	
Materials	Al	Sn	Zr	Mo	Cr	Nb	Fe	Si	C
TC4	6.35	2.04	2.16	2.83	1.55	1.96	0.021	0.06	0.05
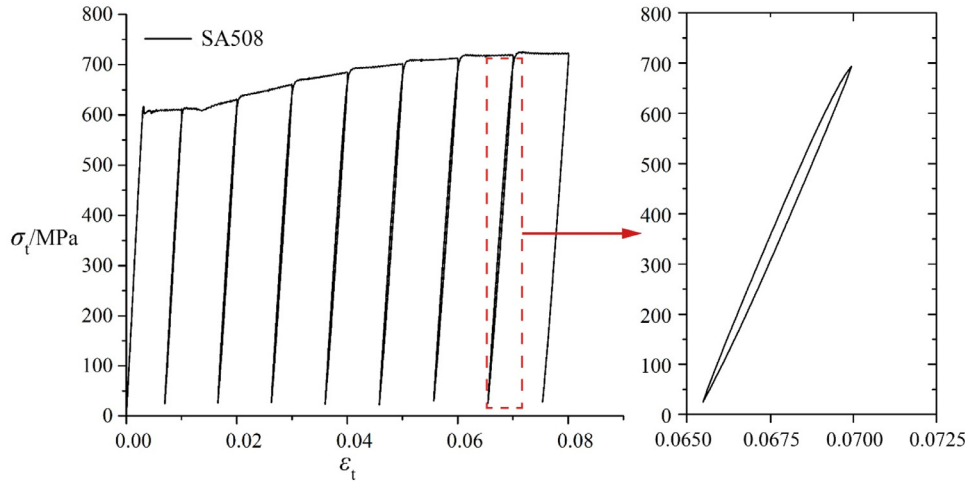
Fig. 5. Illustration of a cyclic uniaxial tensile test.

respectively.

$$K_{IIC} = \sqrt{\frac{E_0}{1 - v^2} J_{SIT}} \qquad (26)$$

$$K_{IC} = \frac{K_{IIC}}{\alpha} \qquad (27)$$

where α is the stress ratio defined as the ratio of maximum shear stress τ_{max} to the maximum normal stress σ_{max} (i.e., $\alpha = \tau_{max} / \sigma_{max}$), and can be considered a constant 0.35 for steel and aluminum alloys [37-39].

3. Experiments

3.1. Experimental materials

Experiments were performed on eight kinds of steels, 15CrMoR (abbreviated as 15Cr), 18MnMoNbR (abbreviated as 18Mn), Q345R, S30408, SA508, KMN-S, SA516, SA533, one aluminum alloy 6061-T651 (abbreviated as 6061), and one titanium alloy TC4. The detailed chemical composition of experimental metals is shown in Table 1.

3.2. Uniaxial tensile tests

The tensile specimens were machined into rod-shaped specimens with a diameter of 10 mm (6 mm for KMN-S) and a gauge length of 50 mm (30 mm for KMN-S) in accordance with the Chinese standard [40]. Strain controlled (set at 0.00025/s) tests were performed on Instron-8803 and the strain was measured by an extensometer. Two kinds of uniaxial tensile tests, monotonic tests and cyclic tests, were performed. For monotonic tensile tests, the specimen was continuously loaded till it broke, and then the area reduction rate ψ was measured to

determine the true fracture strain ε_f with Eq. (28).

$$\psi = 1 - e^{-\varepsilon_f} \qquad (28)$$

For cyclic tensile tests, at least 8 loading-unloading cycles were done before the load reached its maximum (i.e., the tensile strength), after which the specimen was unloaded. An illustration of the cyclic tensile test is shown in Fig. 5.

The reloading curve may not coincide with the unloading one due to the combined effort of back stress and friction stress during glide motions [41], but the phenomenon of the hysteresis loop is almost neglectable with the absence of reverse (compressive) loading. Thus, the difference between unloading and reloading curves was not taken into account in this study, and the reloading curve was considered to be exactly the same as the unloading one. All 10 experimental materials were considered ductile as all their tensile fracture surfaces exhibited 'cup-cone' features.

3.3. Compact tension (CT) tests

Compact tension (CT) specimens were used in the fracture toughness tests for determination of fracture toughness K_{IC}. The detailed configuration of the CT specimens is shown in Fig. 6.

A standard straight through starter-notch (WEDM manufactured) was used, and the pre-cracking was performed on an electromagnetic resonance high frequency fatigue testing machine with the stress ratio and frequency set at 0.1 and 150 Hz, respectively. During pre-cracking, the fatigue crack length was measured every 20k cycles until it was about 1.3 mm. To meet the standard requirement [42], side grooves with a 1.5 mm depth and 90° angle, were made on both sides of the CT specimen after pre-cracking. A single CT specimen with 35 cycles was used
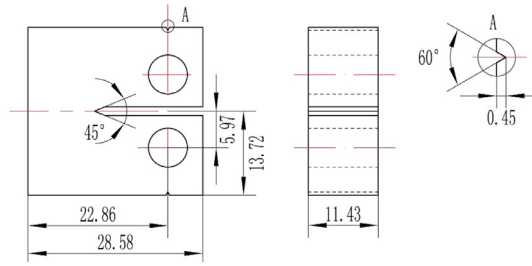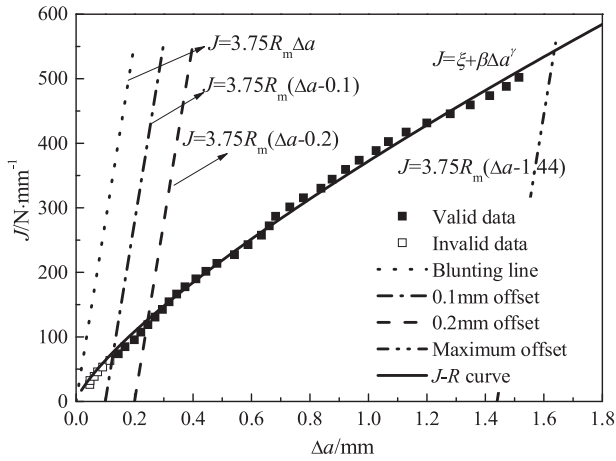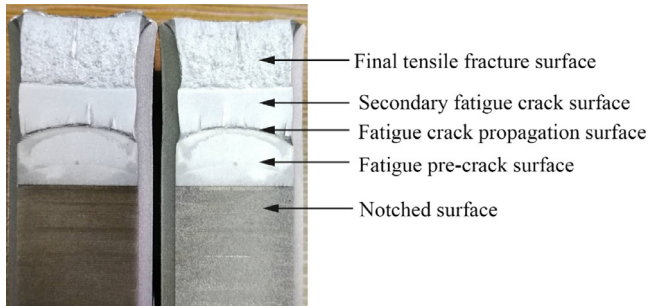
Fig. 6. Configuration of the CT specimen.

Fig. 7. Illustration of the *J-R* curve.

Fig. 8. Illustration of the macro-fracture surface of a CT specimen.

Fig. 9. Stress-Strain Microprobe (SSM) system B4000.

3.4. Spherical indentation tests (SITs)

Specimens were machined into $10 \times 10 \times 50$ mm blocks by Wire cut Electrical Discharge Machining (WEDM). Then, the indentation surface was gradually ground by 180–320–600–800–1200 mesh sandpapers, and eventually polished with 2.5 μm diamond spray. The SITs were performed on the Stress-Strain Microprobe (SSM) system B4000 (Advanced Technology Company), as shown in Fig. 9. A tungsten carbide spherical indenter (the Young's modulus E_{ind} and Poisson's ratio v_{ind} of which were 710 GPa and 0.23, respectively) with a radius R of 0.38 mm was used in SITs. Indentation tests were displacement controlled, and the maximum indentation depth was set at 0.24R (including 8 equal-depth interceptions). Illustrations of the load-depth curves for all experimental materials are in Fig. 10.

4. Finite element analysis

Finite element (FE) calculations were performed in this study to investigate the reasonability of IEF and to determine the amount of pile-up (or sink-in) during a SIT. Taking the characteristics of SITs into consideration, an axisymmetric model was developed in Abaqus/Standard, as shown in Fig. 11. The specimen was regarded as a cylinder with both radius and height 2.16 mm in FE calculations, and the symmetrical properties were set at the symmetric axis while the displacement along the loading direction was restricted at the bottom surface (as shown in Fig. 11). Five different indenter radii were tried, $R = 0.1, 0.2, 0.3, 0.38$ mm (corresponding to the spherical indenter used in SITs), and 0.5 mm. The spherical indenter was modeled as an elastic body with the mechanical properties from the indenter used in SITs. For investigations on the reasonability of IEF, the mechanical properties used in specimen modeling were from uniaxial tensile tests on SA508, while for determination of h_c, stress-strain data were from SITs with Eqs. (6) and (7).

Surface-to-surface contact with finite sliding was used and the indenter surface was considered as the master surface. A four-node bilinear axisymmetric element in 'full integration' CAX4 was used, and the friction coefficient was set at 0.2 according to our previous studies [29, 43]. The mesh around the contact region was refined, and three mesh sizes, 0.004, 0.002, and 0.001 mm, were tried. From the sensitivity study on mesh size (with $R = 0.1$ mm spherical indenter) shown in Fig. 12, it was found that the mesh size does not have a significant influence on the overall development of load-depth curve, but effects their smoothness, and the application of 0.002 mm meshes yielded a calculation with neglectable difference from even finer meshes. Therefore, 0.002 mm was used for meshes around the contact region, and the specimen consisted of about 52,000 elements.

The FE calculation was displacement controlled with maximum indentation depth set at 0.2R (in accordance with $\varepsilon_p = 12\%$), and the

to determine the *J-R* curve and the construction line was defined as

$$J = 3.75R_m \Delta a \tag{29}$$

where Δa and R_m are the crack extension and tensile strength, respectively. A *J-R* curve is shown in Fig. 7, in which the effective data was described with Eq. (30).

$$J = \xi + \beta \Delta a^\gamma \tag{30}$$

where ξ, β, and γ are all coefficients that need to be determined.

The intersection of a line parallel to the construction line at an offset value of 0.2 mm and the *J-R* curve was used as J_{IC} of the material. Then, the fracture toughness K_{IC} was calculated with Eq. (18). After the completion of all 35 cycles, secondary fatigue cracking was performed on the CT specimen to mark the crack propagation, and then the specimen was continuously loaded until it broke. An illustration of the macro-fracture surface of a CT specimen is shown in Fig. 8. The fatigue pre-crack length and the crack propagation were measured to verify whether the test met the requirements in GB/T 21143-2014 [42].
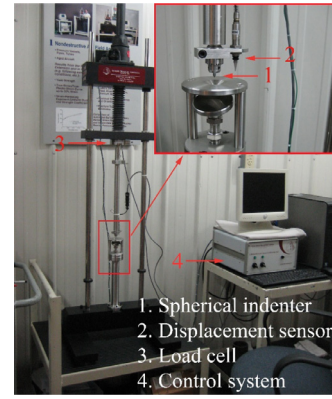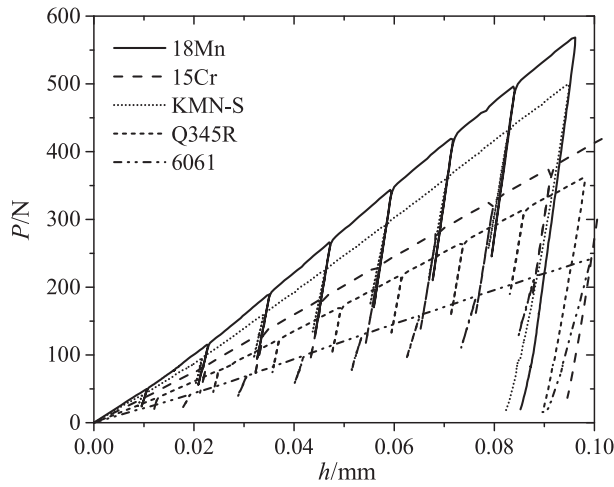
Fig. 10. Illustration of the load-depth curves from cyclic SITs.
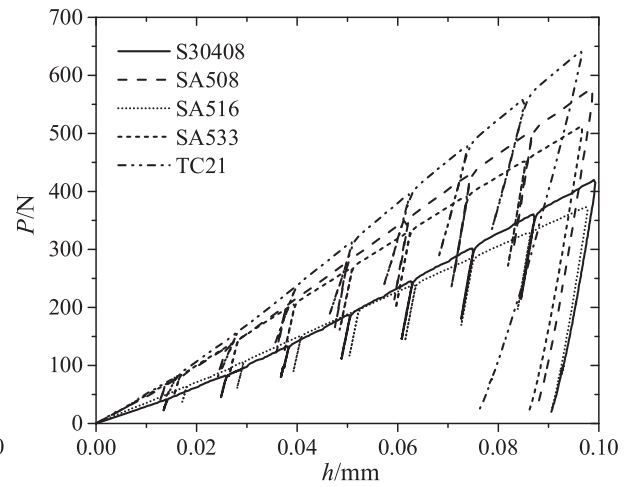
Fig. 11. FE modelling of the SIT.

Fig. 12. Sensitivity study on mesh size.

Table 2
Mechanical properties from conventional destructive tests.

Materials	E_0	$R_{p0.2}$	R_m	Ψ	K_{IC}
18Mn	207	678.65	742.38	0.74	223.01
15Cr	180	387.73	540.36	0.80	140.00
KMN-S	205	592.15	606.41	0.76	195.82
Q345R	207	344.15	505.21	0.81	176.80
S30408	181	250.96	697.26	0.78	174.60
SA508	207	540.12	675.38	0.68	201.80
SA516	205	336.32	500.61	0.74	159.76
SA533	207	535.98	665.67	0.73	186.30
6061-T651	72	251.54	295.32	0.67	54.28
TC4	111	891.49	951.66	0.58	89.97

determined through an average value of two tests and the K_{IC} was from the average of three CT tests.

5.2. Calculations from SITs

The true stress-plastic strain calculated with Eqs. (6) and (7) is shown in Fig. 13. The data points were fitted with the Holloman constitutive equation shown in Eq. (31).

$$\sigma = E_P \varepsilon_t^n \tag{31}$$

where E_P is the strength coefficient, and n is the hardening exponent. The same critical strain criterion 12% was applied to all experimental metals (except for TC4, with an application of the critical stress criterion 800 MPa), and the fracture toughness K_{IC} from HTM is shown in Table 3.
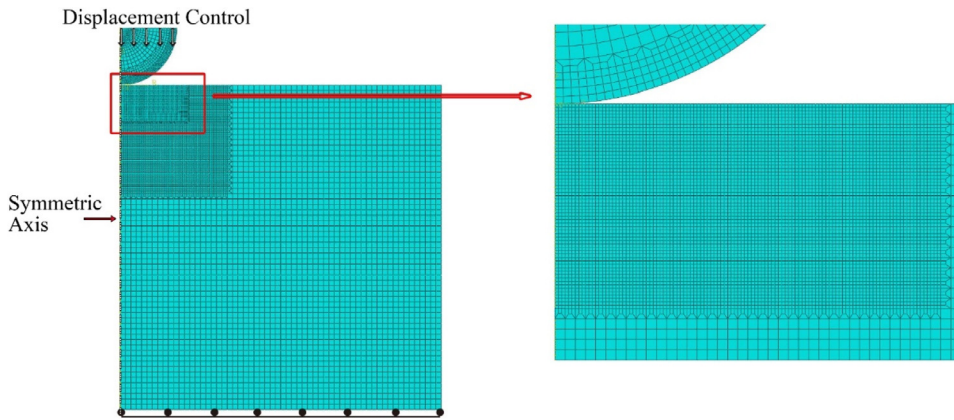
'boundary effect' was neglected in this study as the radius of the specimen was more than 7 times larger than the maximum contact radius $a_{max} = 0.3$ mm (for $R = 0.5$ mm, at $h = 0.1$ mm).

5. Results and discussion

5.1. Conventional test results

The mechanical properties of experimental metals from conventional destructive tests is shown in Table 2, in which the tensile results were
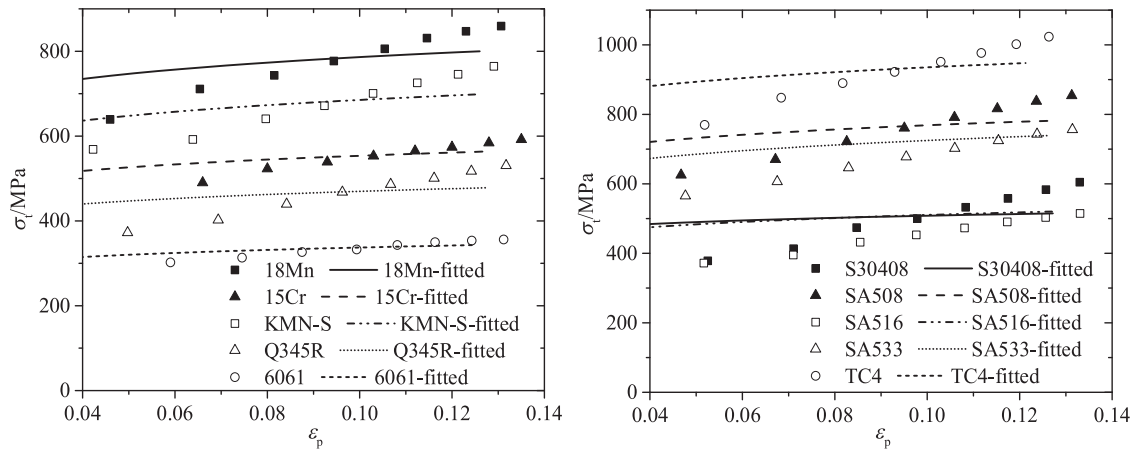
Fig. 13. True stress-plastic strain calculations from SITs.
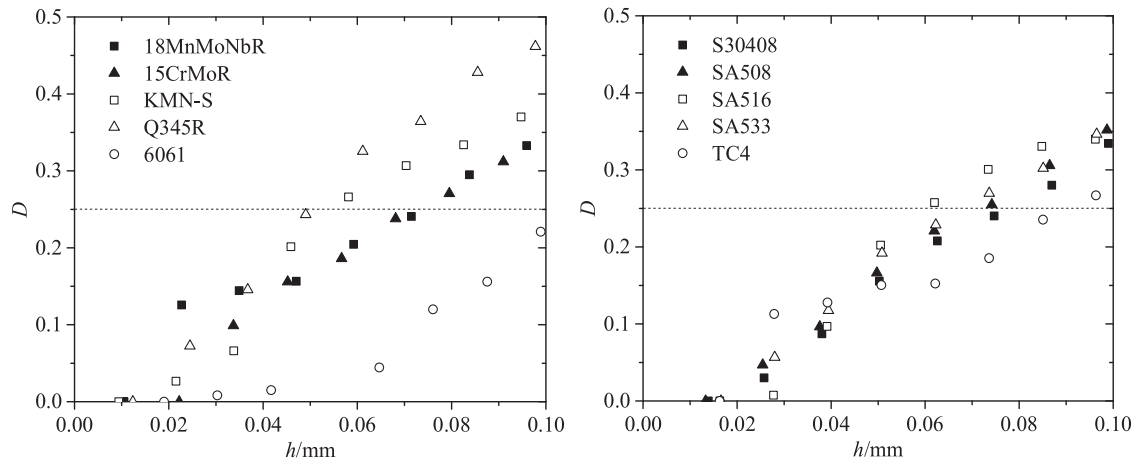
Fig. 14. Damage evolution in SITs.

Table 3
Fracture toughness K_{IC} from the HT model.

Materials	E_0	E_P	n	h_{Cri}	W_{IEF}	K_{IC}	Error/%
18Mn	199	938	0.078	0.076	171.76	261.46	17.24
15Cr	179	658	0.076	0.076	114.45	202.42	44.58
KMN-S	188	831	0.085	0.076	152.12	239.16	22.13
Q345R	190	556	0.074	0.076	102.29	197.16	11.51
S30408	182	576	0.055	0.076	107.47	197.79	13.28
SA508	215	909	0.074	0.076	161.98	263.92	30.78
SA516	213	614	0.081	0.076	113.72	220.10	37.77
SA533	199	879	0.085	0.076	161.82	253.78	36.22
6061	69	404	0.080	0.076	70.78	98.83	82.07
TC4	109	1100	0.073	0.021	34.64	86.90	−3.41

Table 4
Fracture toughness K_{IC} from the CIE model.

Materials	h_{Cri}	W_{IEF}	K_{IC}	Error/%
18Mn	0.074	165.34	256.53	15.03
15Cr	0.072	106.19	194.98	39.27
KMN-S	0.055	102.59	196.40	0.30
Q345R	0.050	59.68	150.59	−14.82
S30408	0.078	110.58	200.63	14.91
SA508	0.072	150.38	254.29	26.01
SA516	0.062	88.68	194.36	21.66
SA533	0.068	141.33	237.17	27.31
6061	0.114	114.45	125.67	131.52
TC4	0.090	227.13	222.52	147.33

It was found that accuracy of the K_{IC} calculation largely depends on the experiment used materials. The calculation model failed (a calculation was considered a failure if it contained more than 30% errors) on the aluminum alloy and four kinds of steels, but succeeded in predicting the K_{IC} of TC4.

An illustration of the damage evolution in SITs is shown in Fig. 14, where a constant critical damage variable $D_{Cri} = 0.25$ was used. The critical indentation depth h_{Cri} was determined through the linear interpolation of two adjacent data points. For 6061, D_{Cri} did not even reached 0.25 at the last cycle, and thus h_{Cri} was determined through an extrapolation (with linear function) of the last two data points. Comparisons in Table 4 proved that the CIE model causes significant errors for both non-ferrous alloys, and the error for steels varied from about a

15% underestimation (for Q345R) to about a 40% overestimation (for 15CrMoR).

The same critical damage variable $D_{Cri} = 0.25$, as that used in the CIE model, was used for determination of the area reduction rate ψ [28]. It deserves noted that an application of the damage variable in area reduction rate determination does not necessarily mean the CSS model is continuum damage mechanics based, and other correlations can also be used to determine ε_f from a SIT. The fracture strain ε_f calculation, as well as the fracture toughness K_{IC} calculated from the critical strain model is shown in Table 5. It was found that ε_f of both non-ferrous alloys could not be calculated with the correlation suggested in the previous study [28], and thus ε_f from uniaxial tension was used as substitutes in the calculation. The comparisons proved that the critical strain model can
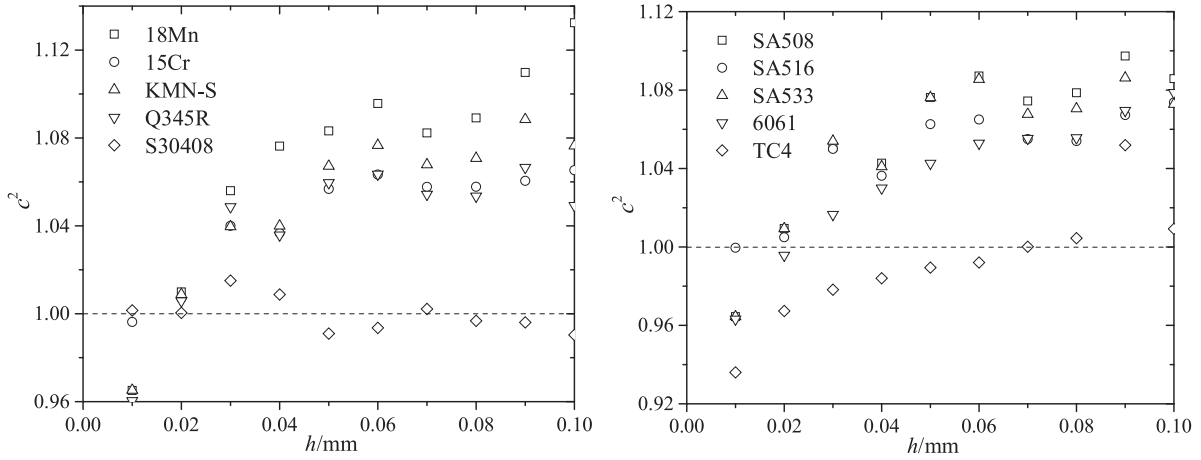
Fig. 15. Variation of pile-up (or sink-in) coefficient c^2 with indentation depth h.

Table 5
Fracture toughness K_{IC} from the critical strain model.

Materials	$R_{p0.2}$	R_m	ε_f	J_{IC}	K_{IC}	Error/%
18Mn	578	712	1.57	1009.88	213.58	−4.23
15Cr	410	501	1.47	668.80	148.48	6.06
KMN-S	490	619	0.89	491.63	137.89	−29.58
Q345R	351	425	0.76	296.68	95.32	−46.09
S30408	409	465	1.79	784.28	161.50	−7.50
SA508	574	696	1.47	932.36	209.84	3.98
SA516	371	462	1.09	452.74	124.59	−22.01
SA533	519	655	1.30	761.92	178.47	−4.21
6061	246	304	–	304.88	61.48	13.26
TC4	729	845	–	682.72	157.47	75.03

Table 6
Fracture toughness K_{IC} from the critical stress model.

Materials	h_{Cri}	J_{IC}	K_{IC}	Error/%
18Mn	0.087	200.94	209.62	−6.00
15Cr	0.100	160.56	177.72	26.94
KMN-S	0.072	141.43	170.93	−12.71
Q345R	0.079	107.56	149.86	−15.24
S30408	0.090	134.73	164.15	−5.98
SA508	0.092	205.82	220.52	9.28
SA516	0.083	126.26	171.91	7.61
SA533	0.088	191.63	204.71	9.88
6061	0.121	122.69	96.45	77.69
TC4	0.139	391.02	219.53	144.00

Table 7
Fitting results for the pile-up (or sink-in) coefficient c^2.

Materials	a_1	a_2	Materials	a_1	a_2
18Mn	1.13760	−0.00252	SA508	1.10676	−0.00178
15Cr	1.07390	−0.00106	SA516	1.07883	−0.00117
KMN-S	1.09660	−0.00165	SA533	1.09238	−0.00134
Q345R	1.07519	−0.00115	6061	1.08931	−0.00201

Table 8
Fracture toughness K_{IC} from the ERR model (with pile-up or sink-in).

Materials	E_0	J_{SIT}	K_{IIC}	K_{IC}	Error/%
18Mn	214	19.63	67.94	194.12	−12.95
15Cr	188	10.07	45.61	130.32	−6.92
KMN-S	194	20.89	66.73	190.67	−2.63
Q345R	192	11.14	48.48	138.52	−21.65
SA508	217	20.25	69.49	198.54	−1.61
SA516	215	9.14	46.47	132.77	−16.89
SA533	203	17.59	62.64	178.97	−3.93
6061	71	5.10	19.95	56.99	5.00

provide an acceptable prediction for 6061, but failed for TC4 and Q345R (with more than 40% errors). However, if the failure of ε_f prediction is taken into consideration, the critical strain model also failed for both non-ferrous alloys. K_{IC} calculation from an application of the critical stress model is provided in Table 6. It can be found that the critical stress model improves the overall accuracy of K_{IC} calculations for steels (with a maximum error from −46.09% to 26.94), but significantly increases the errors in both non-ferrous alloys.

For the HT, CIE, and CSS models, empirical parameters are used as judgments for determination of the critical status, and their values are concluded from SITs without taking the phenomenon of pile-up (and sink-in) into consideration. Therefore, the effect of pile-up (and sink-in) was also neglected in fracture toughness calculations with these three models. However, its effect was considered for the ERR model as no such empirical parameter is used (α used in the ERR model was concluded from conventional tests, e.g., uniaxial tension, rather than SITs). The method we proposed in a previous study [28] was used in determining the amount of pile-up (and sink-in), and the variation of c^2 with

an increasing indentation depth is shown in Fig. 15. It was found that the indentation edge may witness a slightly sink-in at the beginning of a SIT (e.g., the 1st indentation cycle), but c^2 exceeded 1 and significantly increased in the following cycles (except for S30408 and TC4), and the relationship between c^2 and h can be roughly described with the function shown in Eq. (32). The fitting results for all experiment used materials (except for S30408 and TC4) are provided in Table 7, and the effect of pile-up (and sink-in) was neglected for both S30408 and TC4.

$$c^2 = a_1 + \frac{a_2}{h} \tag{32}$$

The A_{eq}-U_D plots (with pile-up or sink-in) of all experiment used metals are shown in Fig. 16. It was found that linear functions, as suggested in the previous study [2], is sufficient in describing the A_{eq}-U_D relation. Therefore, a linear function was used to fit the A_{eq}-U_D plot of each material. The fracture toughness K_{IC} calculated with the ERR model (with an application of the fixed stress ratio 0.35) is shown in Table 8, which proved that the ERR model provides the best K_{IC} calculation among all four models (with a maximum error −21.65%, except for TC4), but failed for TC4 (with a more than 100% error). It was also found that the ERR model provides slightly underestimated K_{IC} for almost all steels (except for S30408), which is preferable in ensuring the safety.
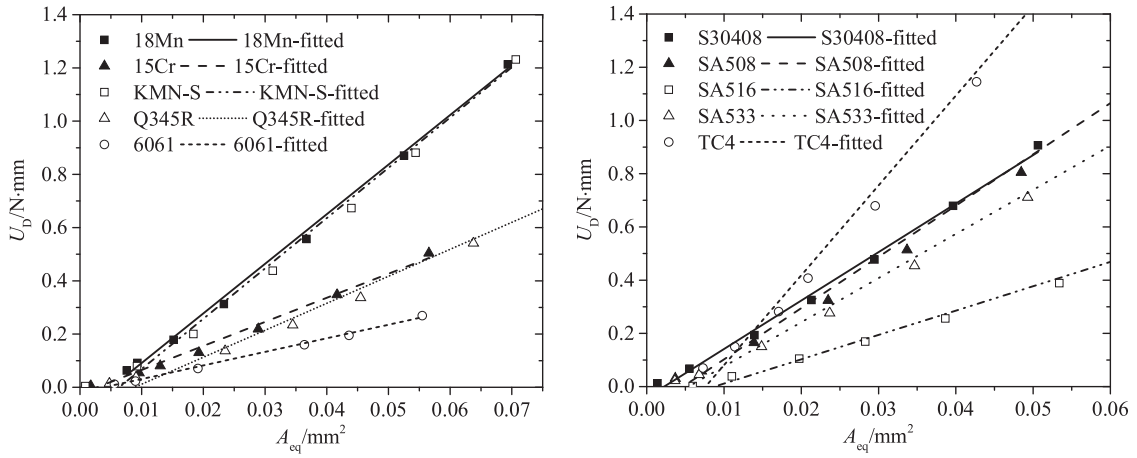
Fig. 16. Illustration of the A_{eq}-U_D plots from SITs (with pile-up or sink-in).

Table 9
Fracture toughness K_{IC} from the ERR model (without pile-up and sink-in).

Materials	J_{SIT}	K_{IIC}	K_{IC}	Error/%
18Mn	21.19	68.07	194.49	−12.79
15Cr	11.65	47.87	136.77	−2.30
KMN-S	21.07	65.98	188.50	−3.74
Q345R	11.54	49.09	140.25	−20.68
S30408	18.75	61.24	174.96	0.21
SA508	20.93	70.32	200.92	−0.44
SA516	9.43	45.41	129.75	−15.98
SA533	17.78	61.73	176.36	−4.37
6061	5.33	20.10	57.44	5.82
TC4	33.74	64.49	184.24	104.78

Despite the fact that an application of the actual depth h_c rather than the measured one h coincides better with the indentation reality, the requirement of FE calculations in c^2 determination complicated the fracture toughness calculation. Therefore, fracture toughness calculations without taking the phenomenon of pile-up and sink-in into consideration are provided in Table 9 as counterparts of the calculations shown in Table 8. The comparison proved that the effect of pile-up (and sink-in) is neglectable in fracture toughness calculations with the ERR model, and this can be understood from the offsetting of sink-in caused E_0 increase (at the 1st cycle) and pile-up caused J_{SIT} decrease (in the following cycles). It deserves noted that, for materials maintain an obvious sink-in phenomenon, both E_0 and J_{SIT} will be over-estimated if the amount of sink-in is not taken into consideration, and this may lead to an aggressive fracture toughness calculation.

6. Error analysis

6.1. Source of errors in the HT model

For the HT model, both the critical stress/strain values and the indentation energy to fracture (IEF) were purely empirical (concluded from experiments on specific materials, e.g., carbon and ferritic steels), and thus may cause errors when applied to other kinds of metals.

The concept of IEF is used in both HT and CIE models, and thus its reasonability was first investigated. For a better understanding of the IEF, the normalized indentation depth h^* (defined as h/R) was used and Eq. (1) can be written as:

$$W_{IEF} = R \int_0^{h^*_{Cri}} p_m \mathrm{d}h^* \tag{33}$$
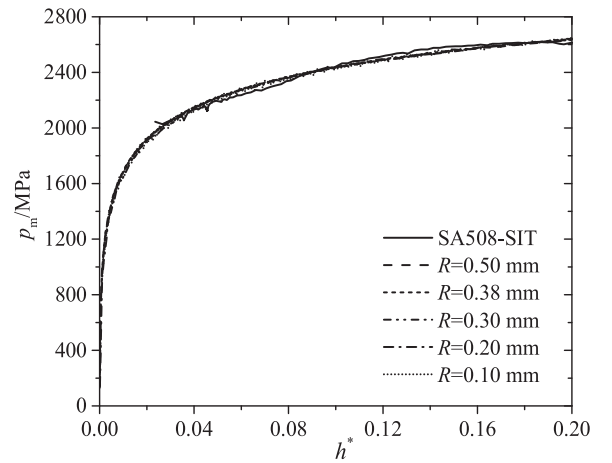

Fig. 17. Comparison of the p_m-h^* curves with an application of different size indenters.

Table 10
Illustration of the optimal indenter size.

Materials	W^*_{IEF}	W_F	R
18Mn	449.93	120.13	0.27
15Cr	299.80	54.44	0.18
KMN-S	398.48	93.53	0.23
Q345R	267.95	75.50	0.28
S30408	281.52	84.21	0.30
SA508	424.31	98.37	0.23
SA516	297.89	62.25	0.21
SA533	423.89	83.84	0.20
6061	185.42	20.46	0.11
TC4	90.76	36.46	0.40

where h^*_{Cri} is the normalized critical indentation depth (defined as h_{Cri}/R). A comparison of p_m-h^* is shown in Fig. 17. Here $\int_0^{h^*_{Cri}} p_m \mathrm{d}h^*$ is defined as normalized indentation energy to fracture and written as W^*_{IEF}. It was found that SITs with different size indenters yield almost the same p_m-h^* curves, and W^*_{IEF} should be the same when different size indenters are used. Therefore, W_{IFE} is closely related to the indenter radius, and the suggested radius ($R = 0.38$ mm) of spherical indenter is nothing more than a coefficient. To investigate the radius that best correlates W^*_{IEF} with K_{IC}, the relationship between W_F and W^*_{IEF} for all experimental materials is given in Table 10, in which W_F was calculated with Eq. (5) (E and K_{IC} from uniaxial tensile and CT tests, respectively)
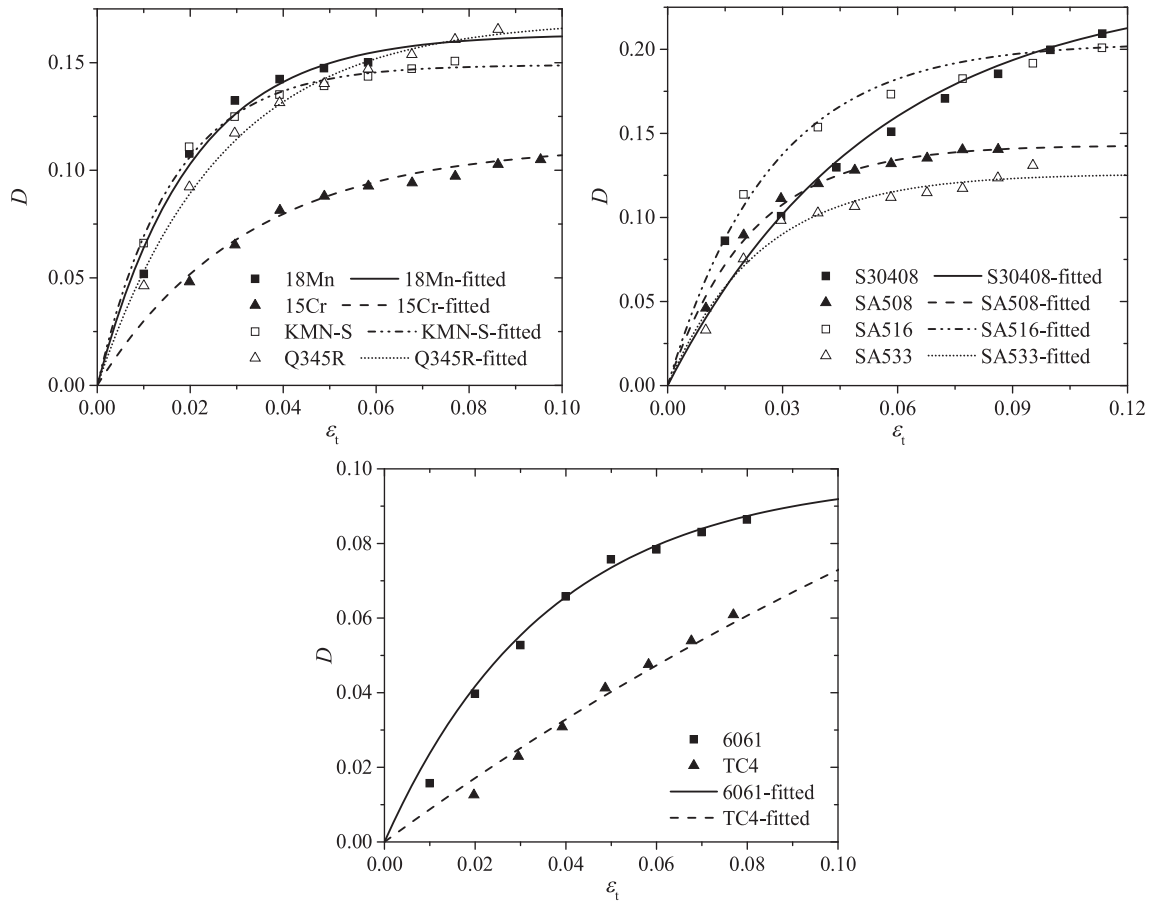
Fig. 18. Illustration of the damage evolution in cyclic uniaxial tensile tests.

and W_{IEF}^* was from SITs. It was found that when W_{IEF} was used, the optimal indenter size (i.e., R in Eq. (33)) varied from 0.18 to 0.30 mm for steels, and even decreased to 0.11 mm for 6061. Therefore, an application of $R = 0.38$ yields an overestimated W_{IEF} (except for TC4).

Additionally, the judgment for determination of the critical indentation depth (i.e., $\varepsilon_p = 12\%$ or $\sigma_t = 800$ MPa), is also purely empirical, and its reliability may be impaired when the specimen material does not exhibit the same mechanical property from which the empirical value was concluded. It should also be noted that as p_m and h^* can be correlated with the representative stress and strain, respectively, as shown in Eqs. (7) and (6), and thus W_{IEF}^* is closely related to the strain energy density in uniaxial tensile tests. Here the tensile energy to fracture W_{TEF} is defined as:

$$W_{TEF} = L \int_0^{\varepsilon_{Cri}} \sigma d\varepsilon \tag{34}$$

where ε_{Cri} is the critical true strain and L is the characteristic length in accordance with the R in Eq. (33). A comparison of Eqs. (34) and (16) proved that the characteristic length L in Eq. (34) equals the critical zone radius ahead of a moving crack tip. However, the purely empirical Eq. (34) does not exhibit as clear a physical meaning as that in Eq. (16), and thus only the universality of the CSS model was discussed.

6.2. Source of errors in the CIE model

For the Critical Indentation Energy to Fracture model, the critical damage variable from uniaxial tensile tests is considered a constant for all materials (0.20 in this study), and thus the critical shear damage variable was a constant 0.25 (calculated with the relationship between D_{Cri}^I and D_{Cri}^{II} shown in Eq. (15)). However, variation of the damage

Table 11
Fracture toughness K_{IC} from the CIE model with an application of the D_{Cri}^I from tensile tests .

Materials	D_{Cri}^I	D_{Cri}^{II}	h_{Cri}	W_{IEF}	K_{IC}	Error/%
18Mn	0.163	0.221	0.065	141.09	236.97	6.26
15Cr	0.112	0.173	0.052	69.83	158.11	12.94
KMN-S	0.149	0.208	0.047	84.92	178.69	−8.75
Q345R	0.170	0.227	0.047	55.05	144.63	−18.19
S30408	0.238	0.291	0.089	131.83	219.06	25.46
SA508	0.143	0.202	0.058	113.88	221.29	9.66
SA516	0.204	0.259	0.073	107.81	214.31	34.14
SA533	0.126	0.186	0.050	98.16	197.66	6.10
6061	0.098	0.160	0.075	69.32	97.81	80.20
TC4	0.213	0.267	0.096	246.60	231.86	157.71

variable from cyclic tensile tests, as shown in Fig. 18, proved that the critical damage variable D_{Cri}^I largely depends on the specimen materials and varies from 0.098 (for 6061) to 0.238 (for S30408). Therefore, it is questionable to use the same critical damage variable in SITs for all metals. Furthermore, it was also found that TC4 exhibited a significantly different damage evolution law (ε_t-D relation, described with a linear function) from all other materials (described with power functions [36]).

The fracture toughness calculated from an application of D_{Cri}^I from tensile tests is shown in Table 11, but it makes little difference on the overall accuracy of the CIE model. As a $R = 0.25$ mm indenter was used when the CIE model was proposed, errors may also be understood from the indenter size effect on W_{IFE} calculations.

Table 12

Fracture toughness K_{IC} from the critical strain model with tensile results.

Materials	ψ	ε_f	W_P	K_{IC}	Error/%
18Mn	0.74	1.35	957.12	223.10	0.04
15Cr	0.80	1.61	746.85	154.06	10.04
KMN-S	0.76	1.43	855.24	200.16	2.22
Q345R	0.81	1.66	705.28	149.98	−15.17
S30408	0.78	1.51	717.86	129.37	−25.90
SA508	0.68	1.14	692.49	174.79	−13.38
SA516	0.74	1.35	563.70	132.56	−17.02
SA533	0.73	1.31	786.68	185.78	−0.28
6061	0.67	1.11	303.51	62.68	15.48
TC4	0.58	0.87	801.77	184.53	105.10
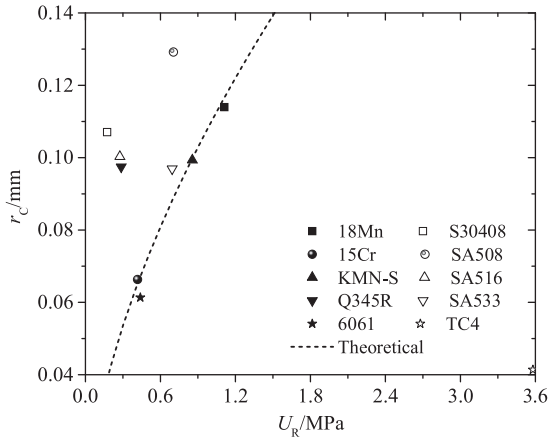
Fig. 19. Illustration of the relation between r_C and U_R.

Fig. 20. Illustration of the J_{Ten} fitted from a cyclic uniaxial tensile test.

Table 13

Fracture toughness K_{IC} from the ERR model with tensile results.

Materials	J_{Ten}	K_{IC}	Error/%	K_{IIC}	α
18Mn	235.96	231.68	3.89	68.07	0.29
15Cr	106.56	145.18	3.70	47.87	0.33
KMN-S	219.96	222.60	13.68	65.98	0.30
Q345R	123.83	167.83	−5.07	49.09	0.29
S30408	166.87	182.18	4.34	61.24	0.34
SA508	208.24	217.64	7.85	70.32	0.32
SA516	141.60	178.60	11.79	45.41	0.25
SA533	158.41	189.83	1.89	61.73	0.33
6061	34.49	52.24	−3.76	20.10	0.38
TC4	280.56	187.65	108.57	64.49	0.34

6.3. Source of errors in the CSS model

For the critical stress one, the definition of J_{IC} was the same as W_{IFE}, and thus it is not discussed. For the critical strain one, calculations were based on assumptions that fracture occurs when the strain energy density ahead the crack tip reaches its critical value, and thus it is also applicable to uniaxial tensile specimens. The fracture toughness calculated from uniaxial tensile tests is shown in Table 12, which proved that calculation errors can be significantly reduced (from −46.09% to −25.90%, except for TC4) with an application of the results from tensile tests. Thus, the critical strain model actually yields more effective calculations than the critical stress one. However, both the stress-strain curve and true fracture strain calculated from a SIT do not exactly the same with those from their tensile counterparts, and thus enlarge errors in the critical strain model. A comparison of ε_f from SITs, shown in Table 5, with tensile ones, shown in Table 12, proved that calculations with an application of the purely empirical correlation proposed in previous study [28] may cause more than 50% underestimation (for Q345R), and even failed for both non-ferrous alloys.

Furthermore, the calculation of critical plastic zone radius r_C, as shown in Eq. (19), in the CSS model is also purely empirical. An illustration of the relationship between r_C and U_R is shown in Fig. 19, where r_C was calculated with K_{IC} from CT tests and tensile properties from uniaxial tensile tests. In Fig. 19, the dotted line is the theoretically derived result from Eq. (19). It was found that the theoretically derived results provide acceptable predictions for only five (18MnMoNbR, 15CrMoR, KMN-S, SA533, and 6061) experimental materials. Actually, there was no clear relationship between r_C and U_R, and the value of r_C varied from 0.041 (for TC4) to 0.129 (for SA508).
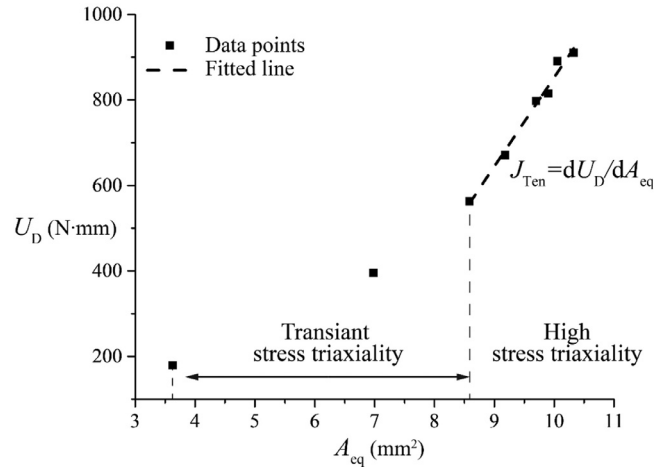
6.4. Source of errors in the ERR model

For the energy release rate model, the energy release rate can also be determined from cyclic uniaxial tensile tests (named as J_{Ten}). An illustration on determination of the J_{Ten} from a cyclic uniaxial tensile test is shown in Fig. 20, which proved that the energy release rate was continuously increased at the beginning of tensile deformation, and this can be understood from the variation of stress triaxiality σ_{Tri} in a tensile specimen. At the beginning of plastic deformation, the specimen was in an idea uniaxial stress state ($\sigma_{Tri} = 1/3$), and when the necking occurred, σ_{Tri} at the necking region exceeded 0.6 [2, 8]. Therefore, there was a transition from intermediate stress triaxiality ($0 < \sigma_{Tri} < 0.4$) to high stress triaxiality ($0.4 \leq \sigma_{Tri}$) during the tensile deformation. Correspondingly, there was a transition from a combination of tensile (damage from debonding of second phase particles) and shear (damage from dislocation pile-up) damage to tensile dominated damage during a tensile test, and the tensile test had an almost constant J_{Ten} after σ_{Tri} reached 0.4. The A_{eq}-U_D plots of all experimental materials are shown in Fig. 21. J_{Ten} from a uniaxial tensile test should be fitted from the later parts of a tensile test (with an almost linear relation between A_{eq} and U_D, as shown in Fig. 21), and J_{Ten} should correspond to the energy release rate from a Mode I fracture test. The fracture toughness K_{IC} can be determined with an application of Eq. (18). Fracture toughness K_{IC} from the ERR model with an application of cyclic uniaxial tensile results is shown in Table 13, where K_{IIC} is from SITs. A comparison on K_{IC} and K_{IIC} proved that the stress ratio α varied from 0.29 to 0.38 (except 0.25 for SA516), and thus an application of $\alpha = 0.35$ may provide a slight deviation on fracture toughness estimations. From Table 13 it was also found that the fracture toughness K_{IC} calculated from a cyclic uniaxial tensile test was also of considerable high accuracy (with a maximum error 13.68%,
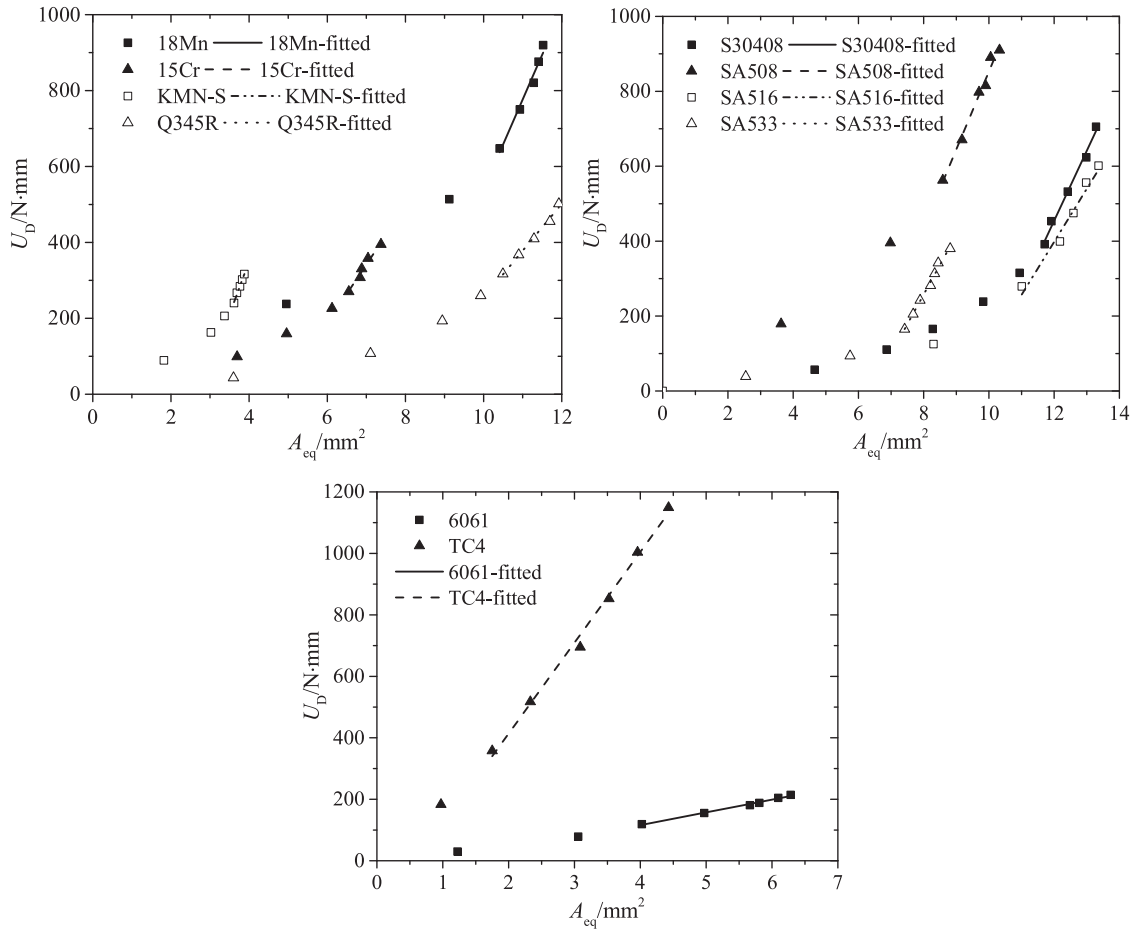
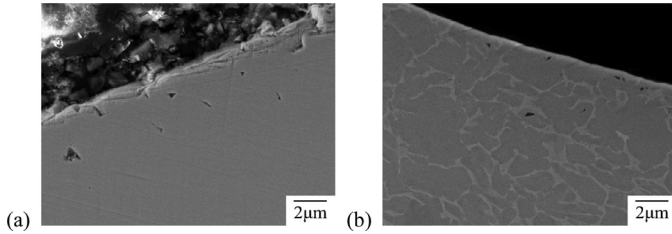**Fig. 21.** A_{eq}-U_D plots from cyclic uniaxial tensile tests.

(a) (b)

Fig. 22. SEM observations of the section surfaces of (a) 6061 (b) TC4 indentation specimens (at $h_{max} = 0.24R$).

(a)

(b)

Fig. 23. SEM observations of the fracture surfaces of (a) 6061 (b) TC4 CT specimens.

except for TC4), and thus the ERR model can also be considered to some extend a universal model for steels and aluminum alloys.

As the empirical value α in the ERR model is valid for both non-ferrous metals, the reason why fracture toughness of TC4 cannot be predicted (while fracture toughness of 6061 can be predicted) with the ERR model was then investigated from their fracture (and damage) mechanisms through scanning electron microscope (SEM) observations. Observation results of the section surface of 6061 and TC4 indentation specimens are shown in Fig. 22(a) and (b), respectively. It was found that wedge shaped voids can be observed in the 'wing region' (region that is about $45°$–$60°$ to the loading axis) of both specimens, and thus both non-ferrous metals used in this study share the same damage mechanism (damage sources from dislocation pile-up) in SITs. This is also consistent with the observations in previous studies [2, 6, 28]. By contrast, the observation results of fracture surfaces of 6061 and TC4 CT specimens, as shown in Fig. 23(a) and (b), respectively, are quite different.
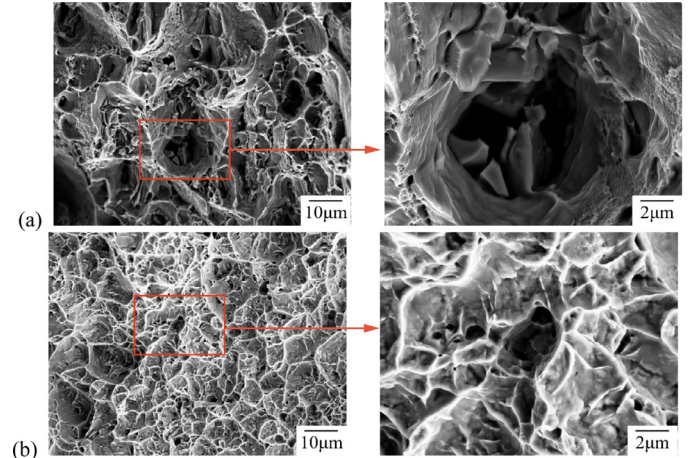
For 6061, its fracture surface is characterized by typical dimple features with second phase particles inside, and the matrix material between the two adjacent dimples experience extensive plastic deformation, which is almost identical with that observed in Mode I fracture surfaces of ductile steels [2, 28], and thus the assumptions in the ERR model is satisfied. For TC4, its fracture surface is also mainly characterized by typical dimple features, and thus it is possible to state that the fracture is a ductile one. However, for titanium alloys with an equiaxed
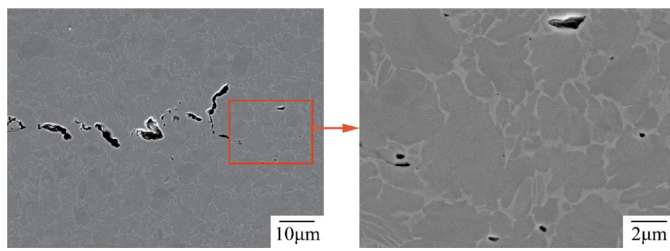
Fig. 24. SEM observations of the section surfaces of TC4 CT specimen.

structure (e.g., the TC4 used in this study), the damage usually initiates at the boundary between α and β phases (there is almost no inclusion in TC4), as shown in Fig. 24, and the crack forms and propagates along the phase boundaries with an exhibition of some partially brittle characteristics. Therefore, TC4 exhibits a different damage evolution law with its 6061 and ductile steel counterparts, as shown in Fig. 18, and assumptions in the ERR and CIE models are not satisfied.

7. Concluding remarks

The paper provides a comparative study on four representative fracture toughness calculation models, the Haggag toughness (HT), critical indentation energy (CIE), critical stress-strain (CSS), and energy release rate (ERR) models, in spherical indentation tests (SITs) through experiments on 10 kinds of ductile metals. The following remarks are concluded from the investigations mentioned above.

(1) Comparisons proved that the none of the four models provide acceptable predictions for all experimental metals. The HT model provided the best fracture toughness K_{IC} calculation for TC4, but failed for 6061 and some steels, while the other three models failed in predicting the K_{IC} of TC4. The ERR model provided an overall acceptable prediction (with a maximum error around 20%, except for TC4) while the maximum errors in the other three models exceeded (or reached) 40% for steels and 6061.

(2) An investigation on the effectiveness of the empirical values used in each model was performed, which proved that the stress ratio exhibits the best consistency for all 10 experimental materials, and thus explains why the ERR model provides the best fracture toughness calculations.

(3) SEM observation of the compact tension specimens proved that both non-ferrous alloys exhibit fracture surfaces with dimple features, which indicate ductile fractures. However, damage generates at boundaries between α and β phases for a TC4 compact tension (CT) specimen, and the crack forms and propagates along the phase boundaries with an exhibition of some partially brittle characteristics. Therefore, both the CIE and ERR models, that developed on continuum damage mechanics of ductile metals, failed in predicting the K_{IC} of TC4.

(4) An application of stress criterion (rather than the strain one) in the CSS model can significantly improve the calculation on steels, but worsens the calculation on both non-ferrous alloys. The strain criterion can also provide reliable calculation (with a maximum error −25.90%, except for TC4) if the fracture strain can be accurately determined (as the tensile results).

(5) Both the strain-energy-density based CSS model and the energy-release-rate based ERR model can be used to calculate the fracture toughness from uniaxial tensile tests, which indicates the universality of these two models.

Acknowledgement

References

[1] Zhang T, Wang S, Wang W. A constitutive model independent analytical method in determining the tensile properties from incremental spherical indentation tests (ISITs). Int J Mech Sci 2018;148:9–19.

[2] Zhang T, Wang S, Wang W. A unified energy release rate based model to determine the fracture toughness of ductile metals from unnotched specimens. Int J Mech Sci 2019;150:35–50.

[3] Li Y, Stevens P, Sun M, Zhang C, Wang W. Improvement of predicting mechanical properties from spherical indentation test. Int J Mech Sci 2016;117:182–96.

[4] Zhang T, Wang S, Wang W. A comparative study on uniaxial tensile property calculation models in spherical indentation tests (SITs). Int J Mech Sci 2019;155:159–69.

[5] Chen H, Cai L-X, Bao C. Equivalent-energy indentation method to predict the tensile properties of light alloys. Mater Des 2019;162:322–30.

[6] Lee JS, Jang JI, Lee BW, Choi Y, Lee SG, Kwon D. An instrumented indentation technique for estimating fracture toughness of ductile materials: a critical indentation energy model based on continuum damage mechanics. Acta Mater 2006;54(4):1101–9.

[7] Bao Y, Wierzbicki T. On fracture locus in the equivalent strain and stress triaxiality space. Int J Mech Sci 2004;46(1):81–98.

[8] Bao Y. Prediction of ductile crack formation in uncracked bodies. Cambridge: Department of Ocean Engineering., Massachusetts Institute of Technology; 2003.

[9] Zener C. Fracturing of metals. Cleveland OH: American Society of Metals; 1948.

[10] Malcher L, Pires FA, De Sá JC. An extended GTN model for ductile fracture under high and low stress triaxiality. Int J Plast 2014;54:193–228.

[11] Nahshon K, Hutchinson J. Modification of the Gurson model for shear failure. Eur J Mech A/Solids 2008;27(1):1–17.

[12] Xue L. Constitutive modeling of void shearing effect in ductile fracture of porous materials. Eng Fract Mech 2008;75(11):3343–66.

[13] Chen Y, Zhang C, Varé C. An extended GTN model for indentation-induced damage. Comput Mater Sci 2017;128:229–35.

[14] Chunyu Z, Yulong Z, Youbin C, Nanfeng C, Lei C. Understanding indentation-induced elastic modulus degradation of ductile metallic materials. Mater Sci Eng A 2017;696:445–52.

[15] Zhang C, Xiao W. Shear-driven damage of ductile metals induced by indentation load. Philos Mag Lett 2015;95(8):401–7.

[16] Banerjee R. Estimation and comparison of fracture toughness of low carbon steel-20MnMoNi55 through ball indentation and fracture testing. Jadavpur University Kolkata; 2013.

[17] He M, Li F, Cai J, Chen B. An indentation technique for estimating the energy density as fracture toughness with berkovich indenter for ductile bulk materials. Theor Appl Fract Mech 2011;56(2):104–11.

[18] Jeon SW, Lee KW, Kim JY, Kim WJ, Park CP, Kwon D. Estimation of fracture toughness of metallic materials using instrumented Indentation: critical indentation stress and strain model. Exp Mech 2016;57(7):1–13.

[19] Li J, Li F, He M, Xue F, Zhang M, Wang C. Indentation technique for estimating the fracture toughness of 7050 aluminum alloy with the berkovich indenter. Mater Des 2012;40:176–84.

[20] Li J, Li FG, Ma X, Wang Q, Dong J, Yuan Z. A strain-dependent ductile damage model and its application in the derivation of fracture toughness by micro-indentation. Mater Des 2015;67:623–30.

[21] Xue FM, Li FG, Li J, He M. Strain energy density method for estimating fracture toughness from indentation test of 0Cr12Mn5Ni4Mo3Al steel with berkovich indenter. Theor Appl Fract Mech 2012;61(1):66–72.

[22] Haggag FM, Byun TS, Hong JH, Miraglia PQ, Murty KL. Indentation-energy-to-fracture (IEF) parameter for characterization of DBTT in carbon steels using nondestructive automated ball indentation (ABI) technique. Scr Mater 1998;38(4):645–51.

[23] Gao X, Jing X, Subhash G. Two new expanding cavity models for indentation deformations of elastic strain-hardening materials. Int J Solids Struct 2006;43(7):2193–208.

[24] Byun TS, Jin WK, Hong JH. A theoretical model for determination of fracture toughness of reactor pressure vessel steels in the transition region from automated ball indentation test. J Nucl Mater 1998;252(3):187–94.

[25] Byun TS, Kim SH, Lee BS, Kim IS, Hong JH. Estimation of fracture toughness transition curves of RPV steels from ball indentation and tensile test data. J Nucl Mater 2000;277(2):263–73.

[26] Murty KL, Mathew MD, Wang Y, Shah VN, Haggag FM. Nondestructive determination of tensile properties and fracture toughness of cold worked A36 steel. Int J Press Vessel Pip 1998;75(11):831–40.

[27] Chaboche JL. Continuum damage mechanics: present state and future trends. Nucl Eng Des 1987;105(1):19–33.

[28] Zhang T, Wang S, Wang W. Improved methods to determine the elastic modulus and area reduction ratio in spherical indentation tests. Mater Test 2018;60(4):355–62.

[29] Zhang T, Wang S, Wang W. Method to determine the optimal constitutive model from spherical indentation tests. Results Phys 2018;8:716–27.

[30] Lee H, Lee JH, Pharr GM. A numerical approach to spherical indentation techniques for material property evaluation. J Mech Phys Solids 2005;53(9):2037–69.

[31] French IE, Weinrich PF. The influence of hydrostatic pressure on the tensile deformation and fracture of copper. Metall Trans A 1975;6(4):785.

[32] Bao Y, Wierzbicki T. A comparative study on various ductile crack formation criteria. J Eng Mater Technol 2004;126(3):314–24.

[33] Shi M, Huang Z, Lu R. Study of the relation between the simple tension damage factor D_{1C} and pure shear damage factor D_{2c}. J Zhejiang Univ 1988;6(22):20–4.

[34] Andersson H. Analysis of a model for void growth and coalescence ahead of a moving crack tip. J Mech Phys Solids 1977;25(3):217–33.

[35] Anderson TL. Fracture mechanics - Fundamentals and applications. CRC Press; 1991.

[36] Lemaitre J. A continuous damage mechanics model for ductile fracture. J Eng Mater Technol 1985;107(107):83–9.

[37] Kim Y, Chao YJ, Lam PS. Numerical simulation of cup-cone fracture in a round tensile bar. In: ASME 2008 Pressure Vessels and Piping Conference. ASME; 2008. p. 53–60.

[38] Siegmund T, Brocks W. A numerical study on the correlation between the work of separation and the dissipation rate in ductile fracture. Eng Fract Mech 2000;67(2):139–54.

[39] Li J, Zhang XB, Recho N. J–Mp based criteria for bifurcation assessment of a crack in elastic–plastic materials under mixed mode I–II loading. Eng Fract Mech 2004;71(3):329–43.

[40] GB/T 228.1-2010, Metallic materials-Tensile testing part 1: method of test at room temperature, Standardization Administration of the PRC, Beijing, PR China; 2010.

[41] Sritharan T, Chandel RS. Phenomena in interrupted tensile tests of heat treated aluminium alloy 6061. Acta Mater 1997;45(8):3155–61.

[42] GB/T 21143-2014, Metallic materials-Unified method of test for determination of quasistatic fracture toughness, Standardization Administration of the PRC, Beijing, PR China; 2014.

[43] Zhang T, Wang S, Wang W. Determination of the proof strength and flow properties of materials from spherical indentation tests: an analytical approach based on the expanding cavity model. J Strain Anal Eng Des 2018;53(4):225–41.